JOURNAL OF COMPUTATIONAL PHYSICS **143,** 159–180 (1998)
ARTICLE NO. CP985958

Multidimensional Upwinding. Part I. The Method of Transport for Solving the Euler Equations

Michael Fey

Seminar for Applied Mathematics, ETH-Zürich, CH-8092, Zürich, Switzerland
E-mail: fey@sam.math.ethz.ch

Received September 25, 1997; revised February 9, 1998

The aim of this paper is to show a new approach towards the discretization of multidimensional conservation laws. The idea of transport associated with the solution of a scalar equation is used for the convective part of the compressible Euler equations. A multidimensional wave structure is derived to model the acoustic part of this non-linear system, that allows infinitely many propagation directions in the numerical method. This provides the basic knowledge to construct a numerical method that does not rely on Riemann solvers. A more general definition of the waves, together with the concept of consistency, enables the design of a number of effective, genuinely multidimensional, methods.

1. INTRODUCTION

The numerical simulation of fluid flow is necessary for various applications. In one space dimension, numerous shock capturing schemes exist to solve the compressible Euler equations that model the inviscid fluid flow.

Most of the methods use the exact or approximate solution of the Riemann problem (RP). This is the solution of the hyperbolic conservation law with piecewise constant initial data separated by a discontinuity. For the Euler equations and some other non-linear systems, an analytic solution can be determined and is used as a building block in most of the methods. The basic idea is due to Godunow [9] but many other approaches with modifications and simplification exist, e.g., the class of total variation diminishing methods (TVD) [21] or essentially non-oscillatory schemes (ENO) [10].

This successful approach relies on the "relative" simplicity of the one-dimensional solution operator which has a finite number of propagation speeds. It is, in principle, possible to define multidimensional Riemann problems with jumps across cell edges. Schultz-Rinne in [18] classifies 2-D RPs under the assumption that only one wave, i.e., the shock, contact

0021-9991/98 $25.00

surface, or rarefaction wave, is allowed for each discontinuity. The complexity of such solutions and the sensitivity to the initial conditions show that it is hopeless to either find an analytic solution for arbitrary data or use these RPs to construct multidimensional methods.

Similar problems arise for other approaches such as flux-vector or flux-difference splitting methods to adapt to multiple space dimensions. The main reason is that the multidimensional form of the Euler equations, unlike the 1-D case, has infinitely many propagation directions. Thus a simultaneous diagonalization of the Jacobian matrix is not possible which complicates a linearisation at the characteristic speeds as in 1-D.

For these reasons, the most popular solution is the dimensional splitting. The one dimensional operator of the projected equations on the coordinate axes or the normals to the cell boundaries of the control volume is used. Dimensional splitting is mostly associated with the multiplicative version, where the 1-D operator is successively applied to each coordinate direction. The special choice of Strang-splitting allows a maximal order of two without a drastic increase of work.

The additive approach uses the "donor cell" and conservative updating. The computation of the flux uses the same 1-D operator as in the multiplicative version but the flux in the directions of the coordinate axes is computed simultaneously, i.e., the operators are connected additively. This leads to a slight reduction of stability, which, by a reduction of the time step, or the CFL number, can be accounted for. Both approaches work surprisingly well for a lot of problems regarding the amount of approximation made, i.e., that the physical propagation directions are not accounted for.

Three different approaches have been taken to design truly multidimensional methods. Guided by the well-known behavior of the scalar conservation law, techniques were derived to interpret this behavior as a combination of 1-D operators. The corner transport upwinding method (CTU) introduced by Collela [3] and used by various other authors [12, 20] represents this behavior by a predictor-corrector time integration method. Here, the predictor step uses a different coordinate direction than the corrector step.

The conservation law package (CLAWPACK) by LeVeque [11, 14] models the same fact by a sequence of Riemann solutions with different initial data. Application of both approaches to the system case is then established by replacing the 1-D scalar operator with the corresponding operators for the system, i.e., the solution of the Riemann problem.

A third approach was initiated by Roe [16]. Here, the flux difference splitting idea is modified for the multidimensional case. On a cell vertex based grid, the fluctuation, i.e., the divergence of the flux, is computed for three of the vertices building a triangle. In the scalar case, the propagation direction is unique and can be used to update the surrounding vertices in an upwinding manner. In the system case, the fluctuations have to be decomposed and wave models are needed to distribute them in a physical way (see [15, 17] for examples).

In this paper we first formulate an exact solution operator in integral form for the linear equation with constant and variable coefficients. The numerical method is then derived as a proper approximation to this operator without destroying the multidimensional character.

In the second part, we derive a multidimensional propagation operator for the sonic waves of the Euler equations. The Monge cone, i.e., the envelope of all characteristic hypersurfaces, is used as propagation directions. This allows for infinitely many directions in the method. Finally the transported quantities are derived which completes the numerical scheme. A new interpretation of the idea of flux vector splitting coincides with the method and generalizes the splitting approach to several space dimensions.

The third part of the paper summarizes the properties of the method. Necessary conditions for consistency are derived for the numerical contribution or "fluxes." They allow the separation of the form of the contributions from the physical intuition that generated them. From this point of view, modifications of the contributions can then easily be checked and subsequently they lead to a whole class of schemes. Some examples are given.

In Part II [5] of this series, the simplified versions of this approach are used to extend the method to high order accuracy.

2. THE SCALAR CONSERVATION LAW

In this section we will briefly describe the idea of transport that is closely related to the exact solution of a scalar multidimensional conservation law. This was first exploited by van Leer in [13] for the constant coefficient case and investigated in detail in [8] for the non-linear inviscid Burger's equation. Simultaneously, Collela used this idea as the basis for his approach [3] of the CTU method. The CLAWPACK method designed by LeVeque [11] is also based on this idea and puts it in the framework of a solution of Riemann problems. The work of Childs and Morton [2] relates this behavior to the finite element context.

All the approaches start with the exact solution of the linear advection equation

$$u_t + \vec{a} \cdot \nabla u = 0$$

which can be formulated as

$$u(\vec{x}, t) = u(\vec{x} - t\,\vec{a}, 0). \tag{1}$$

In a finite volume discretisation, the average value u_i^n in domain $V_i \subset \mathbb{R}^N$ is defined as

$$u_i^n = \frac{1}{|V_i|} \int_{|V_i|} u(\vec{x}, t_n)\, d\vec{x},$$

where $|V_i|$ denotes the volume of V_i. For the exact solution in (1) and small time steps Δt, we obtain what is sometimes called the "shift and average" routine. The solid lines in Fig. 1

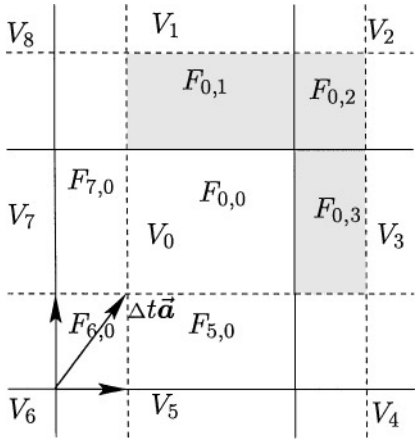

FIG. 1. Propagation of exact solution.

show a finite volume discretisation with the center cell V_0 and the neighbors $V_1 - V_8$. The dashed lines reflect the shifted mesh by $\Delta t\vec{a}$ after time Δt. The new average in V_0 collects all the parts that have moved into the cell. If we define by

$$F_{i,j} = \int_{V_j} u_i(\vec{x} - \vec{a}\Delta t, t)\, d\vec{x}, \qquad \text{with } u_i(\vec{x}, t) = \begin{cases} u(\vec{x}, t), & \vec{x} \in V_i \\ 0, & \text{else} \end{cases} \tag{2}$$

the contributions from domain V_i into V_j, it is clear from the picture, that the average value in V_0 after time Δt is given by

$$u_0^{i+1} = \frac{1}{|V_0|}(F_{0,0} + F_{5,0} + F_{6,0} + F_{7,0}).$$

Thus, for any cell i we get

$$u_i^{n+1} = \frac{1}{|V_i|} \sum_{j \in \overline{NGB}(i)} F_{j,i} = u_i^n - \frac{1}{|V_i|} \sum_{j \in NGB(i)} (F_{i,j} - F_{j,i}), \tag{3}$$

where we indicate the neighborhood of cell i using the term $NGB(i)$, where $NGB(i) = \{j \,|\, j \neq i, \bar{V}_i \cap \bar{V}_i \neq \emptyset\}$ denotes the set of all neighboring indices and $\overline{NGB}(i) = NGB(i) \cup \{i\}$. The second representation of the update in (3) is written as a "flux" difference and yields a conservative method. In comparison, the dependencies for the donor cell approach are sketched in Fig. 2. Flux is computed across interfaces only.

In contrast to the approaches by Collela and LeVeque, where the situation in Fig. 1 is interpreted by one-dimensional operators, we will continue to use the multidimensional representation in (2) and (3) from above. In a more general setting we will allow variable coefficients. The equation becomes

$$u_t + \nabla \cdot (u\vec{a}^T) = 0, \tag{4}$$

where the divergence operator acts on the rows. Formulation (4) is more convenient when moving to systems.

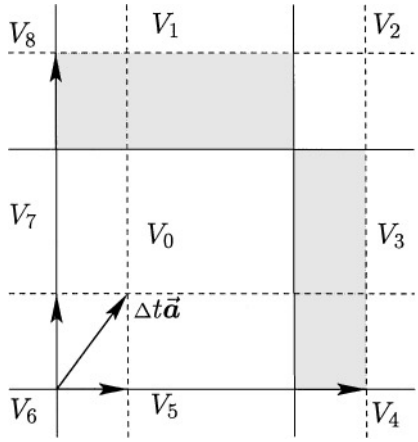

FIG. 2. Dependencies for "donor cell" approach.

To use this approach for non-linear equations, we also have to consider the linear case with variable coefficients. The characteristic curves are then no longer straight lines and the solution is no longer total variation diminishing. With the definition of the function $\vec{z}(\vec{x}, \tau)$ as the solution of the ODE

$$\frac{\partial}{\partial \tau}\vec{z}(\vec{x}, \tau) = \vec{a}(\vec{z}(\vec{x}, \tau)) \qquad \text{and} \qquad \vec{z}(\vec{x}, 0) = \vec{x} \tag{5}$$

as initial value, we can express the behavior of the exact solution governed by

$$\frac{d}{dt}u(\vec{z}(\vec{x}, t), t) = -u(\vec{z}(\vec{x}, t), t)\nabla \cdot \vec{a}(\vec{z}(\vec{x}, t))$$

in terms of an integral as

$$u(\vec{x}, t + \Delta t) = \int_{\mathbb{R}^N} u(\vec{y}, t)\delta(\vec{x} - \vec{z}(\vec{y}, \Delta t))\, d\vec{y}. \tag{6}$$

For Lipschitz continuous $\vec{a}$, (5) has a unique solution for all times and (6) is a representation of the exact solution of (4).

For discontinuous $\vec{a}$, resulting from the approximation of a non-linear equation with piecewise smooth functions, we define

$$u_i(\vec{x}, t, \Delta t) = \int_{\mathbb{R}^N} u_i(\vec{y}, t)\delta(\vec{x} - \vec{z}_i(\vec{y}, \Delta t))\, d\vec{y}, \tag{7}$$

where $\vec{z}_i$ denotes the solution of (5) for the smooth velocity $\vec{a}_i$ continued beyond the cell boundaries of domain V_i.

The flux $F_{i,j}$ is given as

$$F_{i,j} = \int_{V_j}\int_{V_i} u(\vec{y}, t)\delta(\vec{x} - \vec{z}_i(\vec{y}, \Delta t))\, d\vec{y}\, d\vec{x} \tag{8}$$

and the new cell average can be computed as in (3). In smooth regions of the solution Eq. (7) collapses to (6) and the calculation of the flux in (8) reduces to a projection step.

Hence, by approximating (5) and (7) with the proper accuracy, a numerical method of formally any order can be derived. The use of high order reconstruction together with high order integration and quadrature rules lead to the desired accuracy. One advantage of this approach is that the "physics" is captured independently by the characteristic propagation.

Figure 1 suggests that the method is stable as long as the transported quantity remains within the neigboring cells. This defines the maximum time step Δt from

$$\max_i \left| \frac{\Delta t a_i}{\Delta x_i} \right| =: CFL < 1$$

for $\vec{a} = (a_1, \ldots, a_n)^T$ the velocity and $(\Delta x_1, \ldots, \Delta x_N)^T$ the spacing. If $\vec{a}$ depends on space, the *CFL*-number needs to be the supremum over all $\vec{x}$ in the computational domain.

3. MULTIDIMENSIONAL PROPAGATION FOR THE EULER EQUATIONS

In this section we derive the propagation process for the Euler equations. In contrast to other approaches that are based on the approximation with 1-D operators, we seek a multidimensional representation similar to the one for the scalar equation in the previous section.

The shift or propagation process as defined in (1) and (7) heavily use the uniqueness of the propagation direction for each point, in this case $\vec{a}$. A simple extension to systems is possible if they have a finite number of characteristic speeds. This is the case if the full system can simultaneously be diagonalized, which is true by definition for any one-dimensional hyperbolic system. The well-known flux-vector and flux-difference splitting methods are applications of this fact.

Only very few systems retain this property in several space dimensions. Most of them, like the Euler equations, are not simultaneously diagonazable, i.e., the Jacobian matrices of the flux in each of the coordinate axes cannot be diagonalized with the same matrix. In this section we will focus on the propagation first, i.e., the extension of (5) and (7) for the case of infinitely many directions. For this we assume that we know the quantities to be propagated. We postpone their derivation to the next section.

The theory of characteristics provides some information on the behavior of the solution. The characteristic hypersurfaces, extension of the characteristic curves in 1-D, are defined such that an interior operator on the hypersurface can be constructed. Basically, this provides information on the evolution of planar perturbations. Point-wise perturbations propagate along the envelope of all hypersurfaces of the same family.

The Euler equations have two of these envelopes: first, the so-called Monge cone, resulting from the "acoustic" family, associated with the eigenvalues $\vec{k} \cdot \vec{u} \pm c$. This is a true hypersurface unifying infinitely many directions. Second, the envelope of all advective hypersurfaces, associated with $\vec{k} \cdot \vec{u}$, collapse to a single line, the center of the cone. The situation for two space dimensions and time is sketched in Fig. 3. The vector $\vec{k}$ denotes the space-like normal of the characteristic hypersurfaces.

For the second envelope with a unique propagation direction, the flow speed $\vec{u}$, we can directly use the derivation for the scalar equations. Let $\omega(\vec{x}, t) = \omega(\mathbf{U}(\vec{x}, t))$ be one of the components that are propagated with velocity $\vec{u}$. The functional dependence between ω and the vector of conserved quantities $\mathbf{U}$ will be derived in the next section.

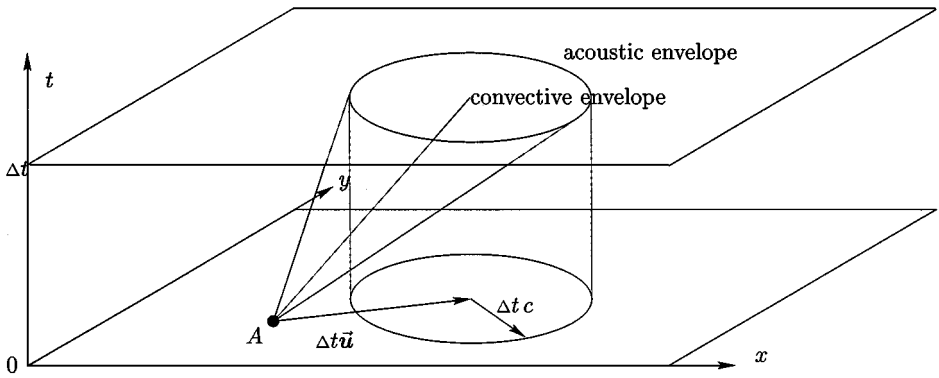

FIG. 3. Forward Monge cone and domain of influence for a perturbation at point A in space-time.

Similar to (5)

$$\vec{z}(\mathbf{U}, \vec{x}, \Delta t) = \vec{x} + \vec{u}\Delta t \tag{9}$$

is the approximation of the characteristic curve for a given velocity field, $\vec{u}(\vec{x}, t) = \vec{u}(\mathbf{U}(\vec{x}, t))$. We define

$$\omega_i^u(\mathbf{U}, \vec{x}, \Delta t) = \int_{\mathbb{R}^N} \omega_i(\vec{y}, t)\delta(\vec{x} - \vec{z}(\mathbf{U}_i, \vec{y}, \Delta t))\, d\vec{y}$$

as the time evolution of ω in cell i along the characteristic curve (9). Contributions to the neighboring cells are defined as

$$\mathbf{F}_{i,j}^u = \int_{V_j} \omega_i^u(\mathbf{U}_i, \vec{x}, \Delta t)\, d\vec{x}, \tag{10}$$

where $\mathbf{U}_i$ denotes the values in cell i.

For the sonic waves the situation is different. This envelope is a true hypersurface with infinitely many propagation directions, assuming that ω is a quantity that is transported according to the Monge cone. Each point on this cone in the $(\vec{x}, t)$ plane with the tip in $(\vec{x}, 0)$ can be reached by

$$\vec{z}(\mathbf{U}, \vec{x}, t, \vec{n}) = \vec{x} + t(\vec{u} + \vec{n}c), \tag{11}$$

where the quantity c denotes the speed of sound, which will be explained in more detail in the next section. The vector $\vec{n}$ denotes a point on the unit sphere $S(1)$. Lacking information, we distribute the quantity ω equally over all points $\vec{z}(\mathbf{U}, \vec{x}, \Delta t, \vec{n})$, $\vec{n} \in S(1)$. With the notation of the previous section we define

$$w^c(\mathbf{U}, \vec{x}, \Delta t) = \frac{1}{|S(1)|} \int_S \int_{\mathbb{R}^N} \omega(\vec{y}, t)\delta(\vec{x} - \vec{z}(\mathbf{U}, \vec{y}, \Delta t, \vec{n}))\, d\vec{y}\, ds. \tag{12}$$

Then, $\omega^c(\mathbf{U}, \vec{x}, \Delta t)$ is the collection of all contributions in space, such that there exist a vector $\vec{n} \in S(1)$ with $\vec{z}(\mathbf{U}, \vec{y}, \Delta t, \vec{n}) = \vec{x}$. The delta function searches backward in time for all points $\vec{y}$, that have a contribution to $\vec{x}$ after time Δt.

For reasons that will become clear in the next section, we need the propagation of a vector valued function in a given direction. Let $\vec{\omega}(\vec{x}, t)$ be a given vector field at time t. We define

$$\omega^{c-}(\mathbf{U}, \vec{x}, \Delta t) = \frac{1}{|S(1)|} \int_S \int_{\mathbb{R}^N} \vec{\omega}(\vec{y}, t) \cdot \vec{n}\delta(\vec{x} - \vec{z}(\mathbf{U}, \vec{y}, \Delta t, \vec{n}))\, d\vec{y}\, ds \tag{13}$$

as the collection of all vectors $\vec{n}$ generated at $\vec{y}$, projected onto $\vec{\omega}(\vec{y}, t)$ and propagated to $\vec{z}(\mathbf{U}, \vec{y}, \Delta t, \vec{n})$. The situation is slightly simpler if we assume $\vec{\omega}$ to be independent of the space variable in a cell as it would be in a piecewise constant representation. Then, it has no influence on the integration and we get

$$\omega^{c-}(\mathbf{U}, \vec{x}, \Delta t) = \vec{\omega} \cdot \frac{1}{|S(1)|} \int_S \int_{\mathbb{R}^N} \vec{n}\delta(\vec{x} - \vec{z}(\mathbf{U}, \vec{y}, \Delta t, \vec{n}))\, d\vec{y}\, ds.$$

The integrals are the collection of all vectors $\vec{n}$ generated at $\vec{y}$ that propagated to $\vec{z}(\mathbf{U}, \vec{y}, \Delta t, \vec{n})$.

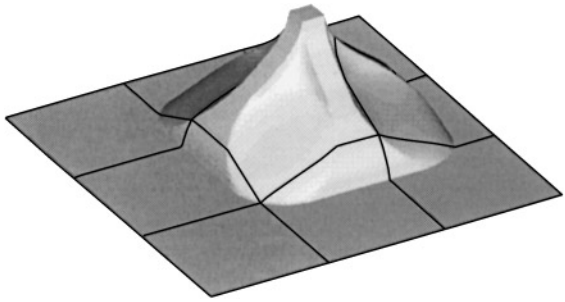

FIG. 4. Function $\omega^c = H_i$ with V_i the center volume.

According to the scalar case and (10) the contributions from one cell to the neighboring cells are given as

$$F^c_{i,j} = \int_{V_j} \omega^c_i(\mathbf{U}_i, \vec{x}, \Delta t)\, d\vec{x} \qquad \text{and} \qquad F^{c-}_{i,j} = \int_{V_j} \omega^{c-}_i(\mathbf{U}_i, \vec{x}, \Delta t)\, d\vec{x}. \tag{14}$$

Figure 4 shows the behavior of ω^c starting with the characteristic function H_i on V_i at time $t = 0$ for ω. The dark lines represent the original rectangular mesh. In addition to the constant motion, the wave changes its shape and grows with Δtc in all directions. The flux is given by integrals over the parts leaving domain V_i as sketched in Fig. 5.

Similar to the scalar case, a direct relation between the neighboring cells exists. The underlying grid only influences the shape of the waves and not their propagation directions. Note that the final method uses a shift and average approach as in the scalar case. The information traveling along characteristic curves is not used to construct the solution as in the contents of characteristics, but to compute the contributions from one domain to an adjacent domain. This retains the finite volume and conservative character of the method which allows shock capturing.

What is left is the definition of ω and $\vec{\omega}$, i.e., the quantity that is actually transported by these processes.

4. THE TRANSPORTED QUANTITIES

What remains to be determined is the actual choice for ω respectively $\vec{\omega}$ in Eqs. (6), (12), and (13). The reader who is only interested in the results may skip to Eq. (17) where the full formulas are given.

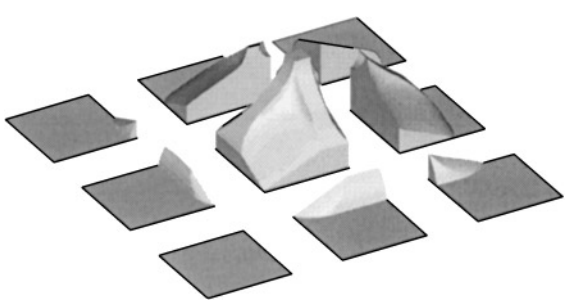

FIG. 5. Contributions from the center cell to its neighbors.

For the derivation of the transported quantities we take a closer look at the flux-vector splitting approach. The multidimensional system can be written as

$$\mathbf{U}_t + \nabla \cdot \boldsymbol{F}(\mathbf{U}) = 0.$$

Here, $\mathbf{U}$ denotes the vector of $N+2$ conserved quantities and $\boldsymbol{F}$ the $(N+2) \times N$ matrix of the multidimensional flux. N is the dimension of the space. Again, the divergence acts on the rows of $\boldsymbol{F}$.

Since the flux-vector splitting uses a 1-D operator, i.e., the Jacobian of the projected multidimensional flux $\boldsymbol{F}$ onto a given direction $\vec{\boldsymbol{n}}$, we can restrict our investigation to the 1-D case, keeping in mind that the results are needed for all vectors $\vec{\boldsymbol{n}}$ on the unit sphere $S(1)$.

In 1-D, the flux $\mathbf{F}(\mathbf{U}) = \boldsymbol{F}(\mathbf{U})$ becomes a vector and is given as

$$\mathbf{F}(\mathbf{U}) = \begin{pmatrix} \rho u \\ \rho u^2 + p \\ u(E+p) \end{pmatrix}, \qquad \text{with } \mathbf{U} = \begin{pmatrix} \rho \\ \rho u \\ E \end{pmatrix}$$

and $p = (\gamma - 1)(E - \rho u^2/2)$, the equation of state. In this notation, ρ denotes the mass density, u the velocity, E the total energy, and p the pressure of the fluid.

The homogeneity of the flux $\mathbf{F}$ allows us to write it as

$$\mathbf{F}(\mathbf{U}) = \boldsymbol{R}\boldsymbol{\Lambda}\boldsymbol{R}^{-1}\mathbf{U}.$$

The matrices $\boldsymbol{\Lambda}$ of the eigenvalues and $\boldsymbol{R}$ of the right eigenvectors can be computed as

$$\begin{aligned} \boldsymbol{\Lambda} &= \operatorname{diag}(\lambda_1, \lambda_2, \lambda_3) = \begin{pmatrix} u-c & 0 & 0 \\ 0 & u & 0 \\ 0 & 0 & u+c \end{pmatrix}, \\ \boldsymbol{R} &= (\mathbf{r}_1, \mathbf{r}_2, \mathbf{r}_3) = \begin{pmatrix} 1 & 1 & 1 \\ u-c & u & u+c \\ H-uc & u^2/2 & H+uc \end{pmatrix} \end{aligned} \tag{15}$$

with c, the speed of sound and H the specific enthalpy, $H = (E+p)/\rho$. It is related to the other quantities by $c^2 = \gamma p/\rho$ in the ideal gas case. It turns out that the vector $\boldsymbol{\alpha}$ has a very simple structure

$$\boldsymbol{\alpha} = \boldsymbol{R}^{-1}\mathbf{U} = \frac{\rho}{2\gamma} \begin{pmatrix} 1 \\ 2(\gamma-1) \\ 1 \end{pmatrix} = \begin{pmatrix} \alpha_1 \\ \alpha_2 \\ \alpha_3 \end{pmatrix}.$$

With the trivial relation

$$\mathbf{U} = \boldsymbol{R}\boldsymbol{R}^{-1}\mathbf{U}$$

we are able to decompose the state vector $\mathbf{U}$ and the flux $\mathbf{F}$ as

$$\mathbf{U} = \boldsymbol{R}\boldsymbol{R}^{-1}\mathbf{U} = \sum_{i=1}^{3} \alpha_i \mathbf{r}_i, \qquad \mathbf{F}(\mathbf{U}) = \boldsymbol{R}\boldsymbol{\Lambda}\boldsymbol{R}^{-1}\mathbf{U} = \sum_{i=1}^{3} (\alpha_i \mathbf{r}_i)\boldsymbol{\lambda}_i.$$

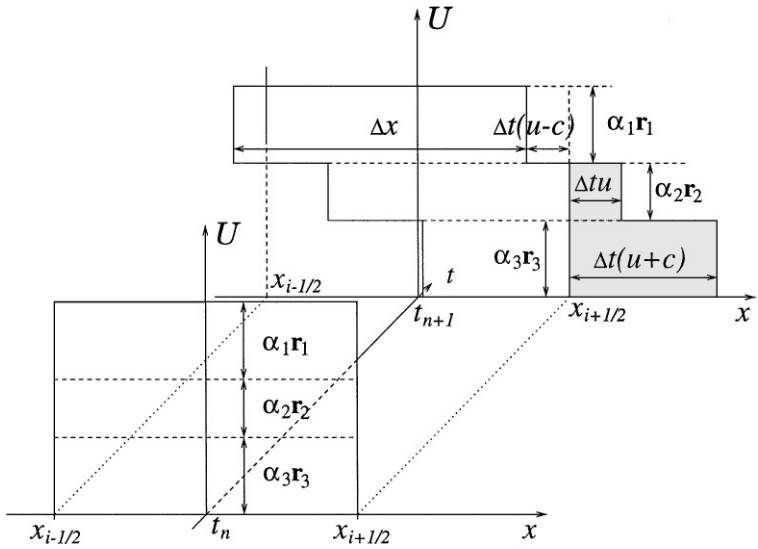

FIG. 6. Decomposition of **U** at time t_n and transport with characteristic speed. The gray region has passed the cell boundary from left to right during time $t_{n+1} - t_n$. Only the right-going flux is indicated.

Thus, the flux can be computed by expanding **U** in terms of the eigenvectors and then transported with the corresponding characteristic speed. This behavior is sketched in Fig. 6. As we have seen in the previous section, the second eigenvalue causes no trouble in the transition to several space dimensions, since the envelope of all characteristic hyper-surfaces collapse to a line. In $\mathbb{R}^N$ we define the vector

$$\mathbf{R}_2 = \frac{\gamma - 1}{\gamma} \begin{pmatrix} \rho \\ \rho \vec{\boldsymbol{u}} \\ \rho |\vec{\boldsymbol{u}}|^2/2 \end{pmatrix}$$

and move each component of $\mathbf{R}_2$ as a scalar quantity described in Sections 2 and 3.

The two distinct acoustic waves propagating with speeds λ_1 and λ_3 will become the surface of the Monge cone and thus be connected in $\mathbb{R}^N$, $N \geq 2$. The connection of these waves can be recognized in the 1-D case. The two eigenvectors $\mathbf{r}_1$ and $\mathbf{r}_3$ are almost equal, except for parts with an opposite sign. The positive part, i.e., $(\alpha_1 \mathbf{r}_1 + \alpha_3 \mathbf{r}_3)/2$, is distributed equally in both (all) directions. This is the behavior we assumed for the process building ω^c. The choices for ω in (12) are the components of

$$\mathbf{R}_1 = \frac{\rho}{\gamma} \begin{pmatrix} 1 \\ \vec{\boldsymbol{u}} \\ H \end{pmatrix}.$$

The part with the opposite sign, i.e., $(\alpha_3 \mathbf{r}_3 - \alpha_1 \mathbf{r}_1)/2$, always has the same sign as the speed of sound c in $u \pm c$. Thus, it points in the same direction as the sonic speed. We associate this quantity with the process (13) generating $\vec{\boldsymbol{\omega}}^{c-}$. The multidimensional extension of $(\alpha_3 \mathbf{r}_3 - \alpha_1 \mathbf{r}_1)/2$ is

$$\boldsymbol{L} = \frac{\rho c}{\gamma} \begin{pmatrix} \vec{\mathbf{0}}^T \\ \boldsymbol{I} \\ \vec{\boldsymbol{u}}^T \end{pmatrix} \tag{16}$$

with $\boldsymbol{I}$ the $N \times N$ identity matrix. The rows of $\boldsymbol{L}$ are used in (13) for $\vec{\boldsymbol{\omega}}$ to compute ω^{c-}.

We now derive the full formulas for the numerical method. The vector $\mathbf{R}_2$ is used in the advection process in (6). We define as the advection wave

$$\mathcal{U}_i(\vec{x}, t, \Delta t) = \int_{V_i} \mathbf{R}_2(\mathbf{U}_i(\vec{y}, t))\delta\left(\vec{x} - \vec{z}_i^u(\mathbf{U}, \vec{y}, \Delta t)\right) d\vec{y} \tag{17}$$

with $\vec{z}_i^u(\mathbf{U}, \vec{y}, \tau)$ solution of

$$\frac{\partial}{\partial \tau}\vec{z}_i^u(\mathbf{U}, \vec{y}, \tau) = \vec{u}_i\left(\vec{z}_i^u(\mathbf{U}, \vec{y}, \tau), \tau\right), \qquad \vec{z}_i^u(\mathbf{U}, \vec{y}, 0) = \vec{y}. \tag{18}$$

The function $\vec{z}$ in (9) is a first order approximation of (18).

The vector $\mathbf{R}_1$ is propagated according to (12) and the first acoustic wave is defined as

$$\mathcal{C}_i^+(\vec{x}, t, \Delta t) = \frac{1}{|S(1)|}\int_{S(1)}\int_{V_i} \mathbf{R}_1(\mathbf{U}_i(\vec{y}, t))\delta\left(\vec{x} - \vec{z}_i^c(\mathbf{U}, \vec{y}, \Delta t, \vec{n})\right) ds\, d\vec{y}, \tag{19}$$

where $\vec{z}_i^c(\mathbf{U},\ \vec{y}, \tau, \vec{n})$ solves

$$\frac{\partial}{\partial \tau}\vec{z}_i^c(\mathbf{U}, \vec{y}, \tau, \vec{n}) = \vec{u}_i\left(\vec{z}_i^u(\mathbf{U}, \vec{y}, \tau, \vec{n}), \tau\right) + \vec{n}c_i\left(\vec{z}_i^u(\mathbf{U}, \vec{y}, \tau, \vec{n}), \tau\right), \qquad \vec{z}_i^u(\mathbf{U}, \vec{y}, 0, \vec{n}) = \vec{y}. \tag{20}$$

The index i indicates the relation of all quantities to the solution within cell V_i with smooth extensions of $\vec{u}$ and c to compute $\vec{z}$ but not in $\mathbf{R}_1$ and $\mathbf{R}_2$.

Using the same hyper-surface in (20) the second acoustic wave becomes

$$\mathcal{C}_i^-(\vec{x}, t, \Delta t) = \frac{q}{|S(1)|}\int_{S(1)}\int_{V_i} \mathbf{L}(\mathbf{U}_i(\vec{y}, t)) \cdot \vec{n}\delta\left(\vec{x} - \vec{z}_i^c(\mathbf{U}, \vec{y}, \Delta t, \vec{n}\right) ds\, d\vec{y}. \tag{21}$$

The constant q needs to be determined through use of the consistency requirement in Section 5. $\mathbf{U}_i(\vec{x}, t)$ denotes a piecewise smooth reconstruction of the solution from the cell averages $\mathbf{U}_i^n$ in cell V_i at time $t = t_n$, i.e., $\mathbf{U}_i(\vec{x}, t_n)$ is an approximation of $\chi_i(\vec{x})\mathbf{U}(\vec{x}, t_n)$ where $\mathbf{U}(\vec{x}, t_n)$ is the exact solution and $\chi_i(\vec{x})$ the characteristic function of domain V_i.

The contribution from domain V_i to one of its neighbors V_j can be computed as

$$\mathbf{F}_{i,j} = \mathbf{F}_{i,j}^u + \mathbf{F}_{i,j}^{c+} + \mathbf{F}_{i,j}^{c-},$$

where

$$\mathbf{F}_{i,j}^u = \int_{V_j} \mathcal{U}_i(\vec{x}, t, \Delta t)\, d\vec{x}, \qquad \mathbf{F}_{i,j}^{c+} = \int_{V_j} \mathcal{C}_i^+(\vec{x}, t, \Delta t)\, d\vec{x}, \qquad \mathbf{F}_{i,j}^{c-} = \int_{V_j} \mathcal{C}_i^-(\vec{x}, t, \Delta t)\, d\vec{x}, \tag{22}$$

and the update to the next time slice is given as

$$\mathbf{U}_i^{n+1} = \mathbf{U}_i^n - \frac{1}{|V_i|}\sum_{j \in NGB(i)} (\mathbf{F}_{i,j} - \mathbf{F}_{j,i}).$$

The formulas are quite cumbersome to compute in this general setting. For the implementation one starts with a piecewise constant approximation for the functions $\mathbf{U}_i(\vec{x}, t_n)$ which allows the analytic integration of (17), (19), and (21) (see Section 6 for more details and relation to existing schemes).

5. CONSISTENCY

Finally, the consistency of the derived discretization has to be checked. This will be done in a more general setting to allow for modifications of the waves. It should be as simple as in the 1-D case. For one spatial dimension, a method is called consistent with the governing equations

$$\mathbf{U}_t + \mathbf{F}(\mathbf{U})_x = 0$$

if the numerical flux $\mathbf{F}_{num}(\mathbf{U}_L, \mathbf{U}_R)$ given for the left and right states $\mathbf{U}_L$ and $\mathbf{U}_R$ equals the physical flux $\mathbf{F}(\mathbf{U})$ for $\mathbf{U} = \mathbf{U}_L = \mathbf{U}_R$, i.e.,

$$\mathbf{F}(\mathbf{U}) = \mathbf{F}_{num}(\mathbf{U}, \mathbf{U}).$$

This, together with a conservative discretization leads to a consistent method.

A comparable criterion will be given for the multidimensional waves derived in Sections 3 and 4. With the same assumption as in 1-D, a uniform solution, the functions $\mathbf{R}_2, \mathbf{R}_1$, and $\boldsymbol{L}$ depend only on the state vector $\mathbf{U}$ and decouple from the spatial variation which is contained in the δ-function. The generalized structure of the waves is

$$\begin{aligned}
\mathcal{U}_i &= \mathbf{R}_2 \, f_i^u(\mathbf{U}_i, \vec{\boldsymbol{x}}, \Delta t) \\
\mathcal{C}_i^+ &= \mathbf{R}_1 \, f_i^c(\mathbf{U}_i, \vec{\boldsymbol{x}}, \Delta t) \\
\mathcal{C}_i^- &= \boldsymbol{L}(\mathbf{U}_i) \cdot \vec{\boldsymbol{f}}_i^c(\mathbf{U}_i, \vec{\boldsymbol{x}}, \Delta t)
\end{aligned}$$

for given functions f_i^u, f_i^c, and $\vec{\boldsymbol{f}}_i^c$.

Since $\mathbf{R}_2$ and $\mathbf{R}_1$ are chosen such that $\mathbf{R}_2(\mathbf{U}) + \mathbf{R}_1(\mathbf{U}) = \mathbf{U}$, a necessary condition is that $f_i^{u,c}$ and $\vec{\boldsymbol{f}}_i^c$ build a decomposition of the state vector $\mathbf{U}$ initially, i.e.,

$$f_i^{u,c}(\mathbf{U}, \vec{\boldsymbol{x}}, 0) = \begin{cases} 1, & \vec{\boldsymbol{x}} \in V_i \\ 0, & \text{else} \end{cases} \qquad \text{and} \qquad \vec{\boldsymbol{f}}_i^c(\mathbf{U}, \vec{\boldsymbol{x}}, 0) = 0.$$

To capture the steady constant solution $\mathbf{U}(\vec{\boldsymbol{x}}, t) = \mathbf{U}_0$ for all time, we need

$$\sum_i f_i^{u,c}(\mathbf{U}, \vec{\boldsymbol{x}}, t) = 1, \qquad \sum_i \vec{\boldsymbol{f}}_i^c(\mathbf{U}, \vec{\boldsymbol{x}}, t) = 0.$$

Summation is over all cells and the conditions have to hold for all $\vec{\boldsymbol{x}}$ in the domain and for all times t. This shows that f^u and f^c need to be partitions of unity. There are two more necessary assumptions that relate the waves to the physical flux.

(a) the centers of mass of the functions f^u, f^c, and $|\vec{\boldsymbol{f}}^c|$ move with velocity $\vec{\boldsymbol{u}}$, i.e.,

$$\vec{\boldsymbol{s}}_i^{u,c}(\tau) := \frac{1}{|V_i|} \int_{\mathbb{R}^N} \vec{\boldsymbol{x}} \, f_i^{u,c}(\mathbf{U}, \vec{\boldsymbol{x}}, \tau) \, d\vec{\boldsymbol{x}} = \vec{\boldsymbol{s}}^{u,c}(0) + \tau \vec{\boldsymbol{u}}(\mathbf{U})$$

$$\vec{\boldsymbol{s}}_i^{c-}(\tau) := \frac{1}{|V_i|} \int_{\mathbb{R}^N} \vec{\boldsymbol{x}} \left| \vec{\boldsymbol{f}}_i^c(\mathbf{U}, \vec{\boldsymbol{x}}, \tau) \right| d\vec{\boldsymbol{x}} = \vec{\boldsymbol{s}}^{c-}(0) + \tau \vec{\boldsymbol{u}}(\mathbf{U})$$

(b) the integration of $\vec{f}^c$ along one of the cell normals $\vec{k}$ gives

$$\int_0^\infty \vec{k} \cdot \vec{f}^c(\vec{U}, \vec{s}_i^{c-}(\Delta t) + h\vec{k}, \Delta t)\, dh = \Delta t c.$$

The first point reflects the fact that the functions $f^{u,c}$ and $\vec{f}^c$ have to follow the mean stream velocity which is fulfilled by construction. All propagation processes in Section 2 have the mean flow velocity $\vec{u}$ as basic ingredient.

The second point determines the amplitude of $\vec{f}^c$ and thus the constant q in (21), since the average of $\vec{f}^c$ always gives zero and cannot be used for this task. This amplitude is related to the presssure part in the flux. Assuming piecewise constant data, the second acoustic wave in (21) simplifies to

$$\mathcal{C}_i^-(\vec{x}, t, \Delta t) = \frac{q}{|S(1)|}\mathbf{L}(\mathbf{U}) \cdot \int_{S(1)} \int_{V_i} \vec{n}\delta(\vec{x} - \Delta t(\vec{u} + \vec{n}c))\, ds\, d\vec{y}.$$

Thus, for the derived method $\vec{f}^c$ has the form

$$\vec{f}^c(\mathbf{U}, \vec{x}, \tau) = \frac{q}{|S(1)|} \int_{S(1)} \int_{V_i} \vec{n}\delta(\vec{x} - \tau(\vec{u} + \vec{n}c))\, ds\, d\vec{y},$$

which in two space dimensions and in the domain $G_{2.1}$ (see Fig. 7) reduces to

$$\vec{f}^c(\mathbf{U}, \vec{x}, \tau) = \frac{q}{2\pi} \begin{pmatrix} \sqrt{1 - \left(\frac{x - \tau u - x_{i+1/2}}{\tau c}\right)} \\ 0 \end{pmatrix}.$$

Applying condition (b) with $\vec{k} = (1, 0)^T$ the x-coordinate axis, we get

$$\int_0^\infty [\vec{f}^c]_1(\mathbf{U}, \vec{s}^c(\tau) + h\vec{k}, \tau)\, dh = \frac{q}{2\pi}\Delta t c \int_{-1}^{1} \sqrt{1 - h^2}\, dh = \frac{q\pi\Delta t c}{2\pi}$$

which shows that $q = 2$ is the correct choice. For N space dimensions, it turns out that $q = N$ is the proper choice which also fits for $N = 1$.

This condition implies that the generated numerical flux in the coordinate directions is consistent with the physical flux, i.e., for two space dimensions with $\boldsymbol{F} = (\mathbf{F}_1, \mathbf{F}_2)$ we have

$$\Delta t \Delta y \mathbf{F}_1 = \mathbf{F}_{1,3} + \mathbf{F}_{0,3} + \mathbf{F}_{5,3} - \mathbf{F}_{2,0} - \mathbf{F}_{3,0} - \mathbf{F}_{4,0}$$
$$\Delta t \Delta x \mathbf{F}_2 = \mathbf{F}_{7,1} + \mathbf{F}_{0,1} + \mathbf{F}_{3,1} - \mathbf{F}_{8,0} - \mathbf{F}_{1,0} - \mathbf{F}_{2,0}.$$

Notation of the volumes and fluxes is as in Figs. 1 and 7.

6. MODIFIED WAVES

The disadvantage of the above approach is the large amount of computational work necessary to compute the contributions. Figure 7 shows the support of the function f^c and $\vec{f}^c$ which needs to be divided into a number of subdomains, each with a different

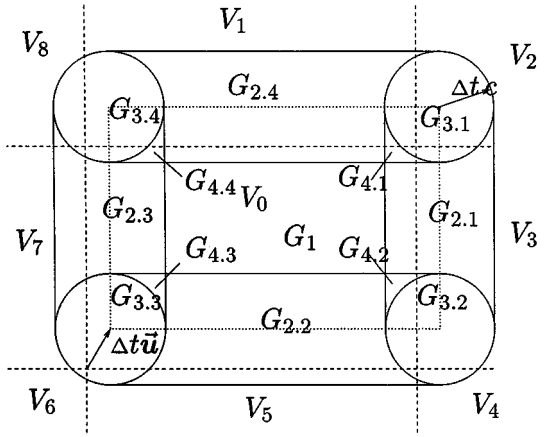

FIG. 7. Support and subdomains for the functions f^c and $\vec{f}^c$ in (23).

representation of the functions. For convenience and to reduce the number of indices we move to a local numeration of the domains. The control volumes are denoted by V_0 for the center cell with indices (i_1, i_2), V_1 the upper cell $(i_1, i_2 + 1)$ and the rest follow clockwise. Note that in most of the previous equations i denotes a multi-index.

The domains G are ordered according to their complexity (in the first version). In G_1 the function is constant, in G_2 there is only one independent variable and in G_3 and G_4 the functions depend on both x_1 and x_2. Subsets are numbered clockwise such that $G_k = \bigcup_i G_{k.i}$.

Since the Monge cone enters into the propagation process (12) and (13) one can notice the circular subdomains and intersections with rectangles. Even though the integration is quite cumbersome, it can be done analytically. As an example, we give a representation of f^c for some subdomains:

$$f^c = \begin{cases} \dfrac{1}{\pi}\arccos\left(\dfrac{x-\Delta tu-x_{i+1/2}}{\Delta tc}\right) & \text{if } \vec{x}\in G_{2.1} \\ \dfrac{1}{2\pi}\left(\arccos\left(\dfrac{x-\Delta tu-x_{i+1/2}}{\Delta tc}\right)+\arccos\left(\dfrac{y-\Delta tv-y_{j+1/2}}{\Delta tc}\right)-\dfrac{\pi}{2}\right) & \vec{x}\in G_{3.1} \\ \dfrac{1}{\pi}\left(\arccos\left(\dfrac{x-\Delta tu-x_{i+1/2}}{\Delta tc}\right)+\arccos\left(\dfrac{y-\Delta tv-y_{j+1/2}}{\Delta tc}\right)-\pi\right) & \vec{x}\in G_{4.1.} \end{cases} \tag{23}$$

In this section for convenience we use the notation $\vec{x} = (x, y)^T$ and $\vec{u} = (u, v)^T$ for the space and velocity vectors. $(x_{i+1/2}, y_{j+1/2})^T$ denotes the upper right corner of a cell. Figure 8 shows one possible example for the computation of the contribution to one of the diagonal neighbors.

The functions f^c and $\vec{f}^c$ are continuous with the direct consequence that the contributions $\mathbf{F}^c$ and $\mathbf{F}^{c-}$ in (14) are differentiable. The wave f^u is discontinuous with the resulting contribution $\mathbf{F}^u$ being only continuous. The influence of this non-differentiable flux is not as severe and reflects the existence of a contact surface, which also only allows a continuous flux.

The functions f^u and f^c share the same properties for consistency. Thus, replacing f^u by f^c in (23) leads to a consistent scheme with a differentiable flux.

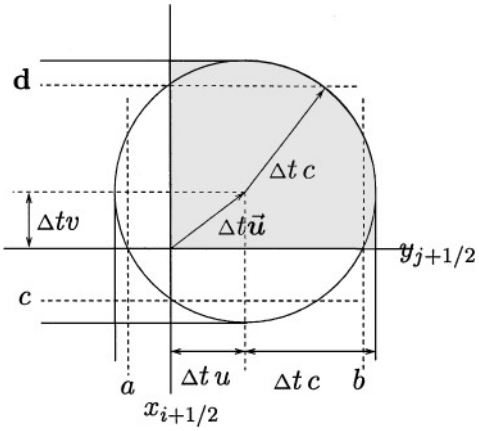

FIG. 8. Integration intervals and shape of domains to compute contribution $\mathbf{F}^c_{0,2}$.

Next, we derive functions f^c and $\vec{f}^c$ that are much simpler and will drastically reduce the amount of computational work. In the spirit of the van Leer flux vector splitting, we use ansatz functions that are piecewise constant, linear, or bilinear. The constraint, to build a partition of unity, defines the function f^c completely. For example,

$$f_i^c = \begin{cases} \dfrac{x_{i+1/2} + \Delta t(u+c) - x}{2\Delta tc} & \text{if } \vec{x} \in G_{2.1} \\ \dfrac{y_{i+1/2} + \Delta t(v+c) - y}{2\Delta tc} \dfrac{x_{i+1/2} + \Delta t(u+c) - x}{2\Delta tc} & \text{if } \vec{x} \in G_{3.1} \end{cases} \tag{24}$$

is a linear function along the edges and bilinear near the corners. The function in the other domains $G_{2.i}$ can be found by symmetry arguments, and in the domains $G_{3.i}$ they are the product of the two functions in the adjacent domains. The second constraint on consistent waves defines the function $\vec{f}^c$. To keep the contributions differentiable we take $f^u = f^c$ as mentioned previously. Figure 9 shows the support for these choices of waves which are

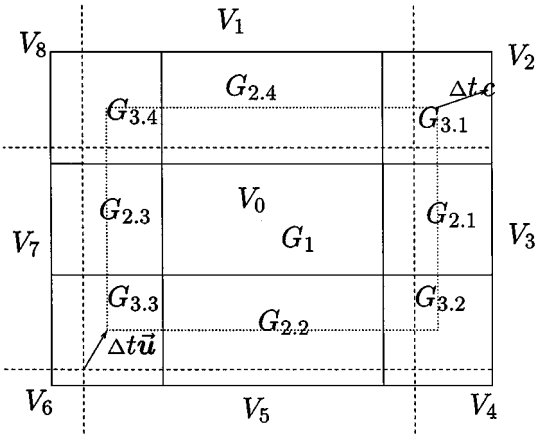

FIG. 9. Support and subdomains for the functions f^c and $\vec{f}^c$ in (24).

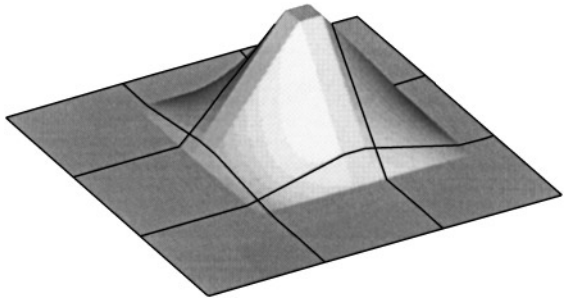

FIG. 10. Function f^c in (24) for $\Delta t = 0.4\Delta x/c$.

now all rectangles. Figure 10 sketches the shape of f^c. This defines a much simpler method with all of the properties of the original version in (23).

Going even further and allowing only piecewise constant ansatz functions on rectangular domains, i.e., the same decomposition of the support as in Fig. 9, leads to the following representation of f^u and f^c:

$$f_i^u(\mathbf{U}_i, \vec{\boldsymbol{x}}, t) = \begin{cases} 1 & \text{if } \vec{\boldsymbol{x}} - \Delta t\vec{\boldsymbol{u}} \in V_i \\ 0 & \text{else} \end{cases}, \qquad f_i^c(\mathbf{U}_i, \vec{\boldsymbol{x}}, t) = \begin{cases} 1 & \text{if } \vec{\boldsymbol{x}} \in G_1 \\ \frac{1}{2} & \text{if } \vec{\boldsymbol{x}} \in G_2 \\ \frac{1}{4} & \text{if } \vec{\boldsymbol{x}} \in G_3 \\ 0 & \text{else.} \end{cases} \tag{25}$$

We omit the representation of $\vec{f}^c$ (for more details see [4, 6, 7]). This is the most efficient method in terms of computational work. It is only 10–20% slower than a van Leer or Steger Warming flux vector splitting method in the donor cell approach and equally fast in the multiplicative operator splitting approach.

Note that for a grid aligned 1-D problem, the method with f in (24) is close to the van Leer scheme while f in (25) gives exactly the Steger–Warming splitting [19].

7. NUMERICAL EXPERIMENTS

The numerical methods derived in the previous section has been tested on a number of problems. The three different versions led to no visible difference in the problems considered. Thus we will show only one of the results. To compare with existing methods, solutions were computed using the Van Leer method with dimensional splitting. Since both methods are of first order, there are only small differences in most of the examples with weak shocks or rarefaction waves. For shock-shock interactions and strong oblique shocks, larger differences can be recognized. Especially noticeable is the influence of numerical viscosity generated by the dimensional splitting. We denote with (MoT) the derived method of transport, and with (VL) the Van Leer flux vector splitting method.

The first example is a two-dimensional Riemann problem. As initial conditions, we choose constant states in each quadrant. Neighboring quadrants are connected by a simple wave, in this case by two slip lines and two rarefaction waves. The initial conditions are

$\rho = 0.5197,$	$p = 0.4,$	$u = -0.6259,$	$v = 0.1$	if $x < 0, y > 0$
$\rho = 0.8,$	$p = 0.4,$	$u = 0.1,$	$v = 0.1$	if $x > 0, y > 0$
$\rho = 1.0,$	$p = 1.0,$	$u = 0.1,$	$v = 0.1$	if $x < 0, y < 0$
$\rho = 0.5197,$	$p = 0.4,$	$u = 0.1,$	$v = -0.6258$	if $x > 0, y < 0.$

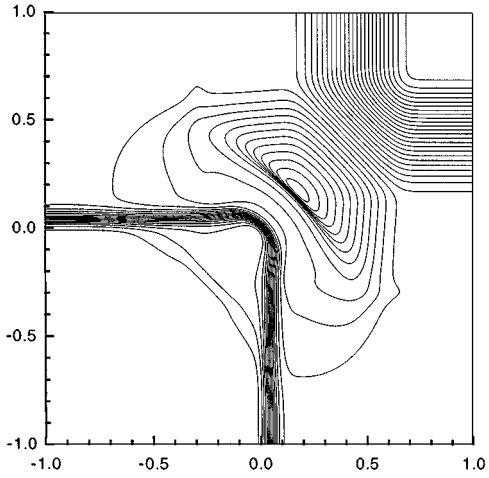

FIG. 11. MoT, Min., 0.2795.

The Cartesian grid used has 400×400 points. The shock thickness, in Figs. 11 and 12 for the MoT and VL, is nearly the same.

The next example includes two weak shocks and two slip lines. The initial conditions are

$$\begin{array}{lllll} \rho = 0.5313, & p = 0.4, & u = 0.0, & v = 0.0 & \text{if } x < 0, y > 0 \\ \rho = 1.0, & p = 1.0, & u = 0.7276, & v = 0.0 & \text{if } x > 0, y > 0 \\ \rho = 0.8, & p = 1.0, & u = 0.0, & v = 0.0 & \text{if } x < 0, y < 0 \\ \rho = 1.0, & p = 1.0, & u = 0.0, & v = 0.7276 & \text{if } x > 0, y < 0. \end{array}$$

A second look at the results (Figs. 13, 14) shows differences in the structure of the shock. The solution of the multidimensional method (Fig. 15) can be interpreted as two Mach reflections and two contact surfaces at the intersection of the four shocks. VL shows one curved shock connected with two others. The density contour lines are circular and the gradient varies only slightly. In the solution of MoT a small density valley moves up to the intersection point.

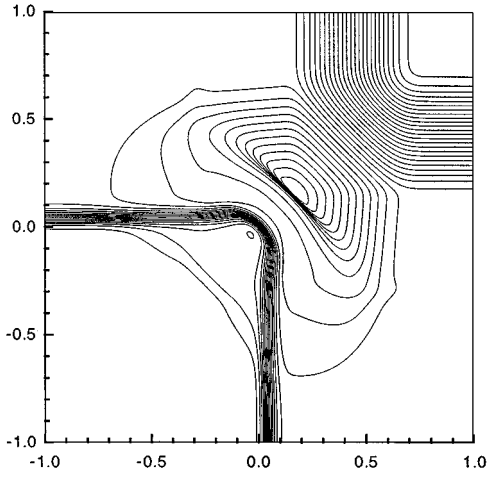

FIG. 12. VL, Min., 0.271.

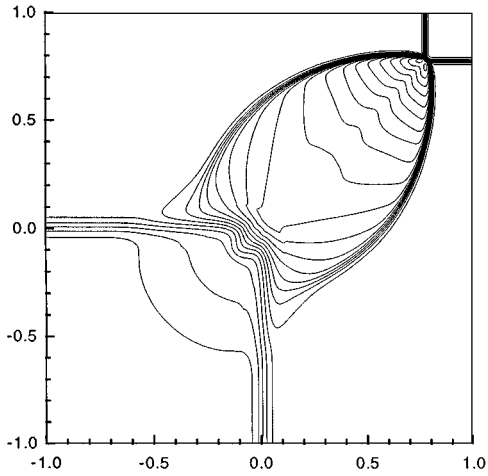

FIG. 13. MoT, Max., 1.721.

There is no exact solution to this problem. However, a qualitative result can be obtained using shock polars [1]. Since the solution is symmetric with respect to the line $x = y$ and self similar, the transformation

$$x' = \frac{1}{\sqrt{2}}(x + y) + st, \qquad y' = \frac{1}{\sqrt{2}}(y - x)$$

puts the shock-shock interaction point at rest, if s is the speed of the shock between quadrant 1 and 3. Since the shock speed is determined from the one-dimensional problems, it is constant in time. Hence, we can use the model of shock reflections as a first approximation. It turns out that, for an angle of 45°, there is no regular reflection. The highest possible angle for these conditions is 40.8°, with a density of 1.835 behind the reflected shock, i.e., a situation as in Fig. 14. Using the 45° angle of incidence, we obtain a Mach reflection with a density of 1.66 behind the reflected shock and 1.52 behind the Mach stem [1]. This seems to indicate that the solution obtained with VL is not well resolved for the same number of

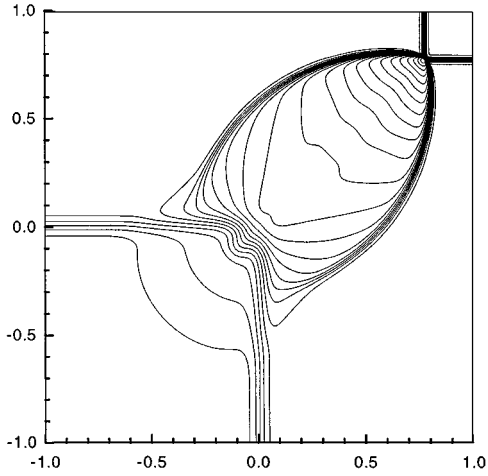

FIG. 14. VL, Max., 1.820.

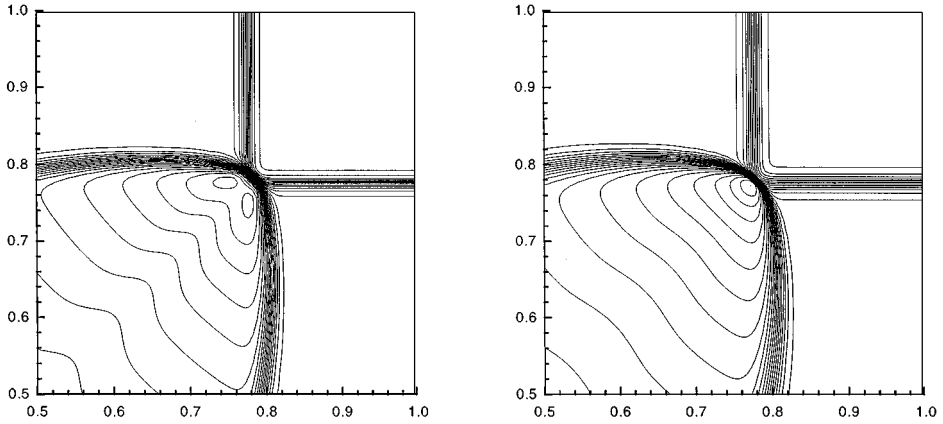

FIG. 15. Enlargement for MoT and VL.

points as MoT that shows the proper behavior. Note that all high order methods produce a result as in Fig. 13.

The spacing $\Delta\rho$ of the iso density contours in the first example (Figs. 11, 12) is $\Delta\rho = 0.02$. In the second example (Figs. 13–15) we used $\Delta\rho = 0.04$.

The last two examples show steady shock reflections. First, we show the solution for the weak Mach 1.4 shock in [3]. The domain is $[-2, 2] \times [0, 1]$ and we use 60×20 points. Figure 16 shows the density at $y = 0.525$. Note that the diamonds in Fig. 16 represent the solution obtained by MoT and show a sharper shock profile than VL. This is surprising since VL has less numerical viscosity than the Steger–Warming method. Figure 17 shows the steady shock profile for the first jump if aligned with the grid. For this 1-D problem MoT is more diffusive than VL as we would expect. This indicates that the dimensional splitting approach introduces more numerical viscosity than the unsplit method.

The last problem includes a strong Mach 10 shock. The values of the analytic solution are shown in Table 1. The domain in this problem is $[-1.73, 4.07] \times [0, 1]$ with a grid 120×20 points. This puts the shock reflection point in $(0, 0)^T$. The observed increase of

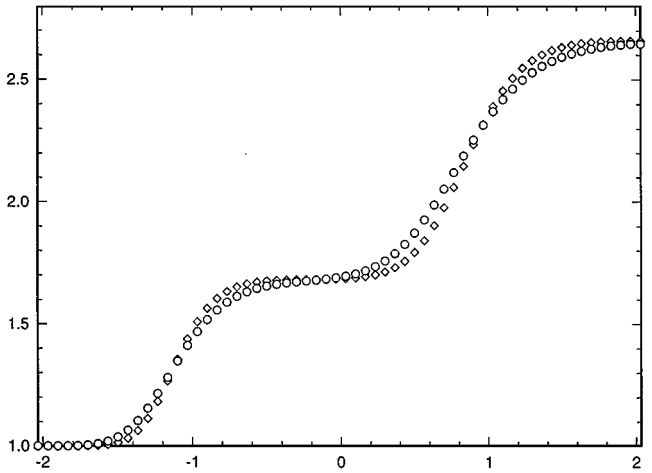

FIG. 16. Comparison of the density profile for the reflection problem along line $y = 0.525$; ◇, MoT; ○, VL.

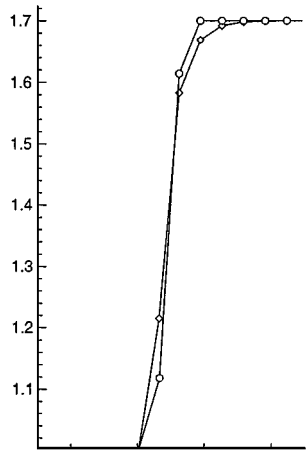

FIG. 17. 1-D density profile for normal shock.

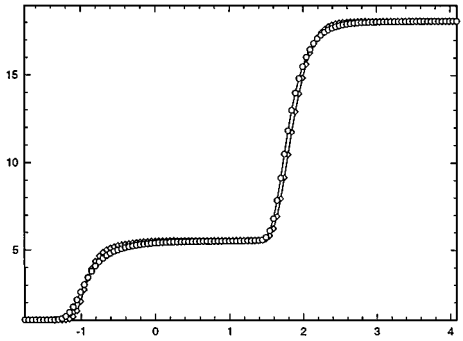

FIG. 18. Density profile for the Mach 10 reflection problem along line $y = 0.525$; $\diamond$, MoT; $\circ$, VL.

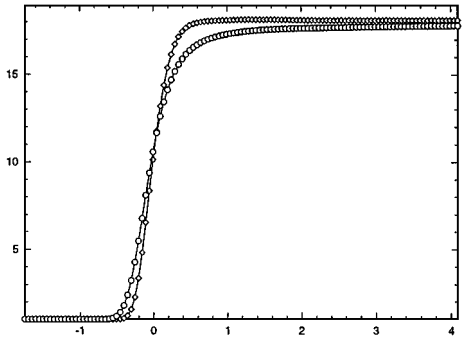

FIG. 19. Density profile for the Mach 10 reflection problem along line $y = 0.0$; $\diamond$, MoT; $\circ$, VL.

TABLE 1

Quantity	Left	Middle	Right
ρ	1.0	5.714285714285714	18.18385326582769
p	1.0	116.5	748.0377039786476
u	23.66431913239847	18.78355331134129	16.70442203362488
v	0.0	−8.453734381916670	1.8e-14

numerical viscosity for VL is more pronounced than in the previous example. Close to the wall, the method is not able to recover the correct jump condition in a reasonable amount of points. We observed the following difference between MoT and VL. Here, MoT shows a much better behavior. The lack of stability for the donor cell approach shows up in this example so that the time step has to be reduced. For comparison, both calculations were done with the reduced time step. This is not necessary for MoT. The solution is the same, even with $CFL = 0.95$. Since the methods used are of first order accuracy only, the obtained results are not very conclusive. Note on the other hand that all high order methods that use flux- or slope limiters reduce to a first order method close to discontinuities. Thus, a better resolution of multidimensional effects is of importance even in the first order part. The influence of the corner contributions is essential for a good representation of strong shocks, as the last two examples indicate. They are of second order only in regions were the solution is smooth.

8. CONCLUSIONS

The method of transport is described by means of the shift and average interpretation. For the scalar equation, this truly multidimensional method can naturally be extended to any order—in contrast to other approaches—where corrections are needed [3] or the structure and velocities of high order waves need to be different from the first order waves [11].

For the case of the Euler equations, a new set of multidimensional waves has been developed to model the physical properties of the linearized equations. Sufficient conditions on the waves are given to ensure the consistency of the numerical method. Three possible modifications have been given to improve some aspects of the original versions. The last version in particular is competitive to other approaches.

Note that $\mathbf{R}_1$, $\mathbf{R}_2$, and $\boldsymbol{L}$ are given functions of $\mathbf{U}$ so that no Riemann problem solution is required. This simplifies the extension to other systems and allows an application even to those systems where the construction of Riemann solutions is difficult, i.e., in geometrical optics or magneto hydrodynamics.

With this information, we are able to construct a mathematical formulation in [5] that shows the extension to high order accurate methods.

REFERENCES

1. Gabi Ben-Dor, *Shock Wave Reflection Phenomena* (Springer-Verlag, New York/Berlin, 1992).
2. P. N. Childs and K. W. Morton, Characteristic Galerkin methods for hyperbolic systems, in *Nonlinear Hyperbolic Equations—Theory, Computation Methods and Applications, Proceedings of the Second International Conference on Nonlinear Hyperbolic Problems, Aachen, FRG, March 14–18, 1988*, edited by J. Ballmann and R. Jeltsch (Vieweg, Wiesbaden, 1989).

3. P. Collela, Multidimensional upwind methods for hyperbolic conservation laws, *J. Comput. Phys.* **87**, 171 (1990).
4. M. Fey, *Ein echt mehrdimensionales Verfahren zur Lösung der Eulergleichungen*, Ph.D. Thesis, ETH Zürich, 1993.
5. M. Fey, Multidimensional upwinding. Part II. Decomposition of the Euler equations into advection equations, *J. Comput. Phys.* **143**, 181 (1998).
6. M. Fey and R. Jeltsch, A simple multidimensional Euler scheme, in *Proceedings of the First European Computational Fluid Dynamics Conference, Brussels, September 7–11, 1992*, edited by Ch. Hirsch (Elsevier, Amsterdam, 1992).
7. M. Fey, R. Jeltsch, and A.-T. Morel, *Multidimensional Schemes for Nonlinear Systems of Hyperbolic Conservation Laws*, Technical Report 95-11, Seminar für Angewandte Mathematik, ETH Zürich, 1995.
8. M. Fey and A. Schroll, *Monotone Split- and Unsplit Methods for a Single Conservation Law in Two Space Dimensions*, Technical Report 57, Inst. für Geometrie und Praktische Mathematik, RWTH Aachen, 1989.
9. S. K. Godunow, Die Differenzenmethode zur numerischen Berechnung von Unstetigkeitslösungen hydrodynamischer Gleichungen, *Mat. Sb.* **47** (1959).
10. A. Harten, High resolution schemes for hyperbolic conservation laws, *J. Comput. Phys.* (1983).
11. J. O. Langseth and R. J. LeVeque, Three-dimensional Euler computations using CLAWPACK, in *Conf. on Numer. Meth. for Euler and Navier–Stokes Eq., 1995*, edited by P. Arminjon.
12. T. Lappas, *An Adaptive Lagrangian Method for Computing 1-D Reacting Flows and the Theory of Riemann Invariant Manifolds for the Compressible Euler Equations*, Ph.D. Thesis, California Institute of Technology, 1993.
13. B. van Leer, Flux-vector splitting for the Euler equations, in *Lecture Notes in Physics* (Springer-Verlag, New York/Berlin, 1982), Vol. 170, p. 507.
14. R. J. LeVeque, High-resolution conservative algorithms for advection in incompressible flow, *SIAM J. Numer. Anal.*, in press.
15. H. Paillère, H. Deconinck, and A. Bonfiglioli, A linearity preserving wave model for the solution of the Euler equations on unstructured meshes, in *ECCOMAS 94* (Wiley, New York, 1994).
16. P. L. Roe, *Linear Advection Schemes on Triangular Meshes*, Technical Report CoA, Rep. No. 8720, Cranfield, 1987.
17. M. Rudgyard, A comparison of multidimensional upwinding for cell vertex schemes on triangular meshes, in *Proceedings of Conference on Numerical Methods for Fluid Dynamics* (Oxford Univ. Press, London, April 1992).
18. C. W. Schulz-Rinne, J. P. Collins, and H. M. Glaz, *Numerical Solution of the Riemann Problem for Two-Dimensional Gas Dynamics*, Research Report No. 92-02, Seminar für Angewandte Mathematik, ETH Zürich, 1992.
19. J. L. Steger and R. F. Warming, Flux vector splitting of the inviscid gasdynamic equations with application to finite difference methods, *J. Comput. Phys.* **40**, 263 (1981).
20. E. F. Toro and S. J. Billet, A unified Riemann-problem-based extension of the Warming–Beam and Lax–Wendroff schemes, *IMA J. Numer. Anal.*, in press.
21. H. Yee, *Upwind and Symmetric Shock-Capturing Schemes*, Technical Report TM 89464, NASA, 1987.